



An Experimental Study of Damage Evolution in Granite Under Compression and Its Influence on Wave Propagation

Tao Zhou¹ · Dongya Han² · Jianbo Zhu¹

Received: 27 March 2022 / Accepted: 25 December 2022 / Published online: 31 January 2023
© The Author(s), under exclusive licence to Springer-Verlag GmbH Austria, part of Springer Nature 2023

Abstract

When subjected to significant loading, damage occurs in rock, leading to degradation of mechanical properties and increased wave attenuation. Although wave propagation in porous and jointed rocks has been extensively studied, influences of damage evolution on wave propagation are not fully understood. In this study, damage evolution and its influence on ultrasonic wave propagation in unconfined uniaxially loaded granite specimens were experimentally investigated. Granite specimen was firstly compressed to a certain load to generate damage and then unloaded immediately. The stress-driven damages in granite specimens during and after loading were quantified by acoustic emission and micro-CT scanning, respectively. Meanwhile, ultrasonic wave propagation in granite specimen along the loading direction was measured during and after loading, respectively. Results showed that the stress-driven damage in granite specimen is highly nonlinear, it increases drastically to the peak when the axial stress approaches the peak point. The stress-driven damage during loading is higher than that after loading. Wave propagation in granite is stress-dependent during compression. Both wave amplitude and velocity increase first and then decrease before the axial stress increasing to approximately 60 and 90% of the uniaxial compressive strength of the granite, respectively. However, compared with wave velocity, wave amplitude is more sensitive to stress and the stress-driven damage. The findings of this study could facilitate a better understanding of the relationship between damage evolution and wave propagation and attenuation in rocks.

Highlights

- The acoustic emission and micro-CT scanning can be adopted to quantify stress-driven damage in granite specimens.
- Wave amplitude is much more sensitive to stress and the stress-driven damage than wave velocity.
- Wave propagation is affected by the competition between the enhancing effect due to closure of initial cracks and the weakening effect due to generation of new cracks.

Keywords Damage evolution · Wave propagation · Acoustic emission · Micro-CT scanning · Damage characterization

1 Introduction

There exist numerous pre-existing defects, such as micro-cracks and voids, in rock. Activation and development of pre-existing defects under external loading are characterized as damage evolution in continuum damage mechanics (Kachanov 1986). Damage evolution not only deteriorates the mechanical behavior of rock but also significantly affects wave propagation and attenuation across it. Although wave propagation and attenuation in porous and jointed rocks have been extensively studied, damage evolution and its influence

✉ Jianbo Zhu
jianbo.zhu@szu.edu.cn

¹ Guangdong Provincial Key Laboratory of Deep Earth Sciences and Geothermal Energy Exploitation and Utilization, Institute of Deep Earth Sciences and Green Energy, College of Civil and Transportation Engineering, Shenzhen University, Shenzhen, China

² School of Resources and Safety Engineering, Central South University, Changsha, China

on wave propagation are not fully understood. Therefore, it is essential to generate and quantitatively characterize damage and to study the effect of damage evolution on wave propagation in rocks (Xie et al. 2020; Zhou et al. 2019).

To date, wave propagation and attenuation in fractured and damaged rocks have received considerable attentions over the years (Ahrens and Rubin 1993; Kaneko et al. 1979; Han et al. 2020; Huang et al. 2014; Li et al. 2015; Meredith et al. 1991; Modiriasari et al. 2018; Pyrak-Nolte et al. 1990; Shirole et al. 2020; Wu et al. 2022; Yang et al. 2020a, b; Zhu et al. 2011). Through studying wave propagation in porous rocks, Shatilo et al. (1998) and Xi et al. (1997) concluded that seismic attenuation grows with increasing porosity. Ai and Ahrens (2007) investigated the effects of shock-induced damage on ultrasonic velocity and attenuation in granite. Their results showed that wave velocity decays exponentially with the normalized distance from the impact source. Recently, Martínez-Martínez et al. (2016) studied the effects of progressive fracture of rocks on wave attenuation. Their results revealed that wave velocity increases until the unstable crack propagation begins and decreases only when rock damage is very high. Zhu et al. (2020) investigated the effects of damage, heterogeneity and waveforms on low-amplitude stress wave propagation and attenuation in damaged rocks. However, understanding of the influence of damage evolution in intact rock specimens on wave propagation is still at its infancy.

To study damage evolution in rocks, the keys are to create rock damage in a controllable manner and to quantitatively characterize it. Currently, there are mainly two methods to create damage in rocks in laboratory. One is to apply a certain load to the specimen to create stress-driven damage (Ahrens and Rubin 1993; David et al. 1999; Tapponnier and Brace 1976; Zhu et al. 2008). Liu and Ahrens (1997) investigated shock-induced damage in San Marcos gabbro via impacting a lead projectile at a velocity of 1.2 km/s. Eberhardt et al. (1999) quantitatively studied stress-driven brittle fracture damage in Lac du Bonnet granite using uniaxial compression tests. The other is to heat rock specimen at a high temperature for a certain time to produce thermally induced damage (Chaki et al. 2008; Yang et al. 2017). Yang et al. (2017) produced thermal damage in granite by exposing the specimens to different high temperatures. However, high-temperature treatment can also change the mineral composition of rocks (Chen et al. 2017). As mineral composition can also affect mechanical properties and seismic response of rocks, the stress-driven damage in rock specimens is preferred.

To quantify damage evolution in rocks, an appropriate damage variable is needed. To date, many damage variables, e.g., elastic modulus, ultrasonic velocity, acoustic emission (AE) and computed tomography (CT) value, have

been proposed to quantitatively assess damage evolution of brittle materials such as rock and concrete. Attributed to the availability and nondestructive characteristics, AE detection and micro-CT scanning are two promising methods that have been used to either qualitatively or quantitatively determine and analyze damage evolution in rocks during and after loading (Kim et al. 2015; Stanchits et al. 2006; Yang et al. 2020a, b).

As AE in rock is mostly produced by microcrack growth, frictional slip and pore collapse (Eberhardt et al. 1999), AE signals detected during rock fracturing can thus be applied to reflect damage during loading. Given this, some scholars adopted AE information to quantify damage evolution in concrete (Iturrioz et al. 2013; Abouhussien and Hassan 2016) and rock (Kim et al. 2015; Liu et al. 2009; Zhang et al. 2015) under compression. For instance, the accumulative AE counts and energy during uniaxial loading were adopted to quantify damage evolution in rocks (Kim et al. 2015; Luo et al. 2020; Zhang et al. 2015).

Besides AE, the X-ray CT technique is a unique and nondestructive method to visualize the defects in opaque materials such as concrete and rock (Renard et al. 2009). In recent years, this technique has been widely adopted to investigate physical properties, failure mechanisms and damage of geomaterials (Feng et al. 2004; Kawakata et al. 1999; Ju et al. 2014, 2018; Zhu et al. 2018). The application of CT has two major advantages. First, through scanning the damaged rock specimen, the three-dimensional crack networks can be obtained from the reconstructed CT images, which provide detailed information for spatial evolution of the micro- and macro-cracks (Kawakata et al. 1999; Renard et al. 2009; Huang et al. 2013). Second, the information conveyed by the CT images, e.g., CT value and gray value, can be applied to quantify damage degree of the specimens (Yang et al. 1998; Feng et al. 2004; Ma et al. 2016).

In this study, unconfined uniaxial loading and unloading test was conducted on granite specimens to generate stress-driven damage. AE activities were monitored and recorded to characterize damage evolution during compression. Then, the unloaded specimens were scanned by an X-ray micro-CT scanner to determine the stress-driven damage after loading and unloading processes. Ultrasonic wave propagation (i.e., wave velocity and amplitude) in granite specimens along the loading direction was measured during and after compression. The influence of stress-driven damage on wave propagation during and after loading was analyzed with the obtained laboratory measurements. Finally, the relationship between damage evolution and wave propagation was discussed. The findings of this study could facilitate a better understanding of the relationship between damage evolution and wave propagation in rocks.

Table 1 Physical and mechanical properties of the granite

Rock type	Density (kg/m ³)	V (m/s)	E (GPa)	Porosity	ν	σ_c (MPa)	σ_t (MPa)
Granite	2642	4355	64	0.7%	0.25	168	8.2

V is the average longitudinal wave velocity, E and ν are the Young's modulus and the Poisson's ratio, σ_c and σ_t are static compressive strength and tensile strength, respectively

2 Experimental Setup

2.1 Specimen Preparation

Granite from a quarry in Hunan, China was tested in this study. The granite consists of 39.3% quartz, 21.4% microcline, 19% biotite, 17.9% plagioclase and 2.4% chlorite. The grain size ranges from 0.1 mm to 2.0 mm with an average of about 0.8 mm. The physical and mechanical properties of the granite are listed in Table 1. The diameter and length of the specimens are approximately 49 mm and 100 mm, respectively. A total of 23 specimens without obvious surface microcracks were tested in this study. All specimens were ground and polished to ensure a surface roughness smaller than 0.02 mm.

2.2 Testing Apparatuses and Method

The experimental setup is shown in Fig. 1. Uniaxial compression tests were conducted on an MTS 647 hydraulic wedge grip machine with a displacement control mode. The uniaxial force was applied at a constant displacement rate of 0.075 mm/s. An AE detection sensor and a PCI-2 AE data-collecting system were used to detect and record AE events during the entire loading process. AE signals were amplified by 40 dB using preamplifiers from Physical Acoustic Corporation. The AE signal acquisition rate was 1.0 MHz with a threshold trigger value of 40 dB. Ultrasonic wave propagation in the granite specimen was measured with an assembly device that consists of an Olympus 5077PR square wave pulser, a Tektronix digital phosphor oscilloscope 2012B and a pair of wave transducers with central frequency of 1.0 MHz. During loading, AE activities and ultrasonic wave

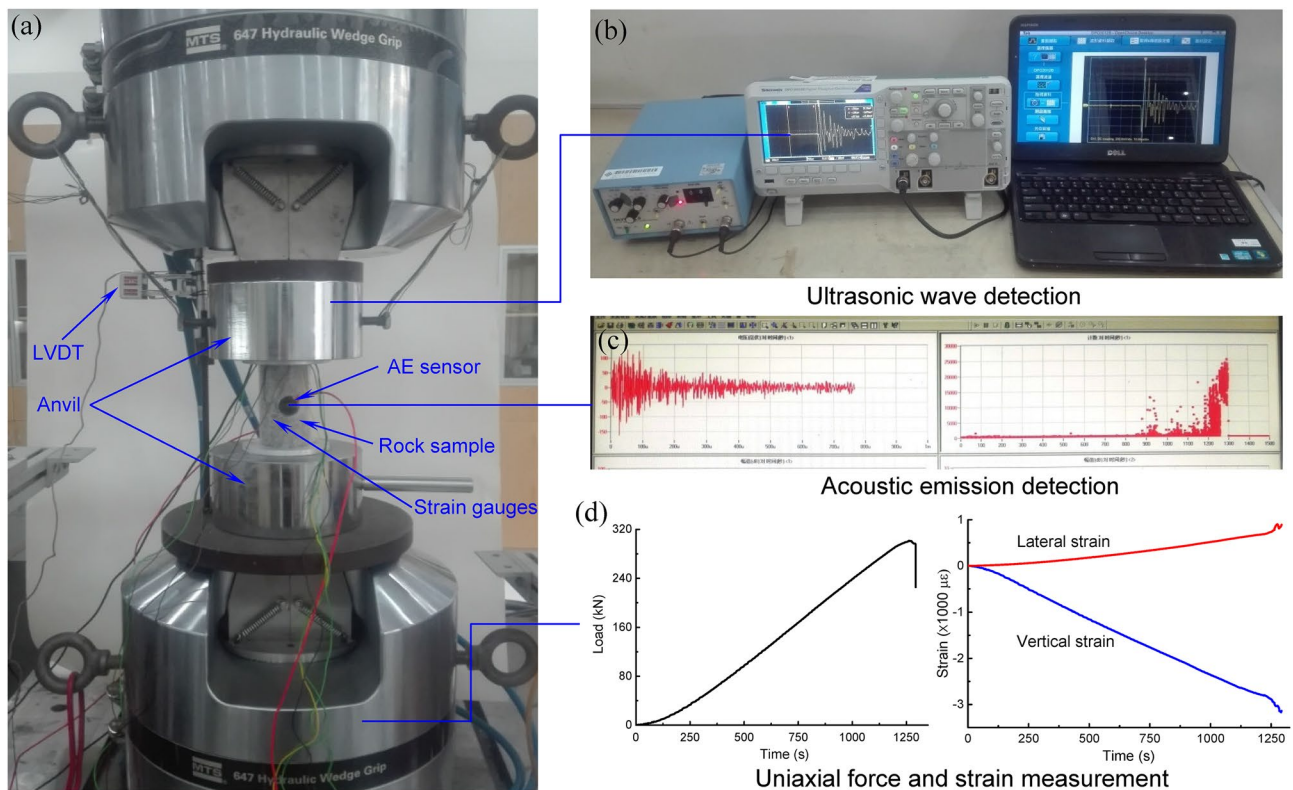


Fig. 1 Experimental setup of wave propagation measurement and AE detection during unconfined uniaxial compression: **a** The MTS 647 hydraulic wedge grip loading machine; **b** Ultrasonic system; **c** acoustic activities monitoring system; **d** uniaxial force and strain measurement

propagation in granite specimens along the loading direction were monitored and recorded.

To evaluate the influence of the stress-driven damage on wave propagation, the granite specimens were firstly loaded to different stress levels, as shown in Table 2. The stress level was specified as a percentage of the uniaxial compressive strength (UCS) of the granite. The specimen was immediately unloaded after loading to the targeted stress level. During loading, AE activities were monitored and recorded for characterizing stress-driven damage evolution. After unloading, micro-CT scanning was performed on the unloaded specimen to determine stress-driven damage after loading and unloading processes. In addition, to examine the effect of the stress-driven damage on wave propagation, ultrasonic wave propagation through the specimen along the loading direction was measured at different stress levels during and after loading processes.

3 Results

3.1 Wave Propagation in Granite During Compression

3.1.1 Waveform

Figure 2 shows the transmitted waveforms through a typical specimen at different stress levels. Notably, the waveforms in Fig. 2 are actual amplitudes of the initial arrival waveforms obtained from the superimposed transmitted waves using the tapering method (Pyrak-Nolte et al. 1990; Zhao et al. 2006). With increasing axial stress, the wave travel time first decreased before increasing at a critical axial stress of approximately 120 MPa, i.e., about 70% of the UCS. In contrast, as the axial stress increased, the peak-to-peak amplitude of the initial arrival wave gradually increased before decreasing. The critical axial stress for this transition is approximately 90 MPa, i.e., 55% of the UCS. The duration of the initial arrival wave was continuously shortened with the increase in axial stress.

Table 2 Change of wave velocity and wave amplitude after uniaxial compression

Sample	UCS%	Wave velocity (m/s)			Wave amplitude (V)		
		V_0	V'	ΔV (%)	A_0	A'	ΔA (%)
G-1	19.9	4603	4812	4.54	3.24	3.4	4.94
G-2	20.1	4697	4922	4.79	3.08	3.18	3.25
G-3	21.5	4487	4621	2.98	3.26	3.44	5.52
G-4	40.2	4414	4553	3.14	2.68	2.92	8.96
G-5	39.9	4342	4504	3.73	3.24	3.64	12.35
G-6	43.7	4406	4689	6.43	3.01	3.26	8.30
G-7	57.9	4394	4686	6.64	2.88	3.29	14.24
G-8	57.8	4460	4698	5.33	2.92	3.25	11.30
G-9	59.2	4496	4767	6.02	3.18	3.70	16.35
G-10	73.6	4220	4562	8.12	3.06	3.53	15.36
G-11	73.5	4295	4640	8.02	2.68	3.15	17.54
G-12	75.5	4439	4740	6.80	1.48	1.69	14.21
G-13	76.4	4376	4749	8.52	2.28	2.71	18.86
G-14	78.3	4515	4916	8.87	3.16	3.80	20.25
G-15	82.0	4338	4766	9.86	3.08	3.68	19.48
G-16	81.3	4373	4727	8.10	1.96	2.44	24.49
G-17	87.1	4242	4705	10.91	2.88	3.12	8.33
G-18	91.5	4376	4661	6.52	2.56	2.62	2.34
G-19	93.0	4373	4732	8.22	2.66	2.74	3.01
G-20	97.1	4385	4497	2.57	3.48	1.8	-48.28
G-21	100	4423	3990	-9.79	2.76	0.0126	-99.54
G-22	100	4416	4055	-8.18	2.92	0.0004	-99.99
G-23	100	4410	4011	-9.05	3.28	0.028	-99.15

V_0 and V' represent wave velocity before and after loading, respectively; A_0 and A' refer to the peak amplitude of the initial arrival wave before and after loading, respectively; ΔV and ΔA are changes of wave velocity and amplitude after loading, respectively

Fig. 2 Transmitted initial arrival waveforms through a typical rock specimen under different loading stresses. The black arrows indicate the arriving time of the initial arrival wave

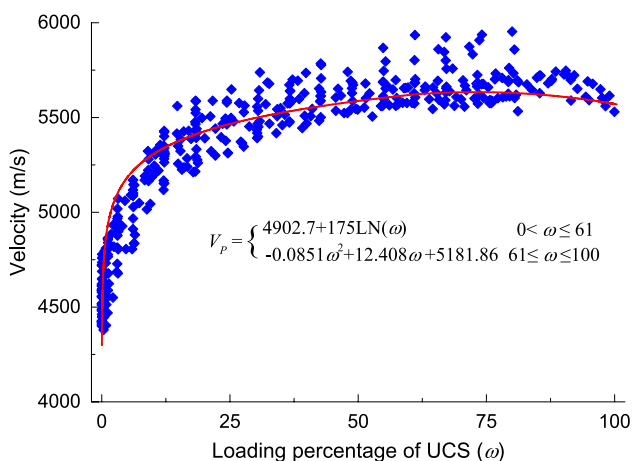
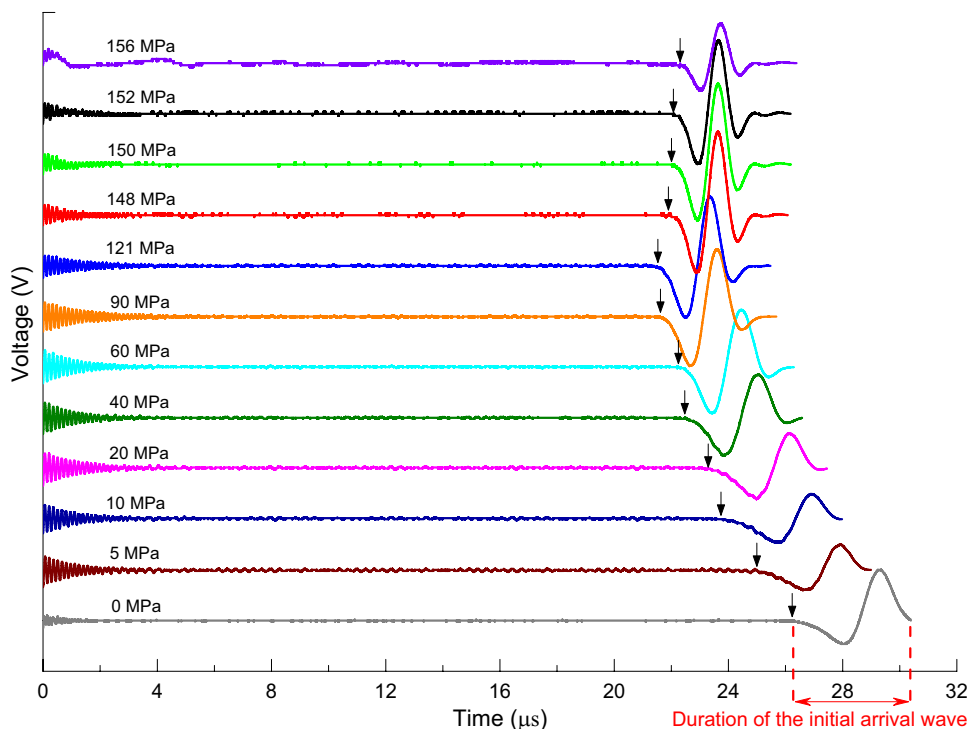


Fig. 3 Change of wave velocity with compressive loading percentage during compression

3.1.2 Wave Velocity

Figure 3 summarizes the relationship between wave velocity of the granite specimen and axial stress during loading process. The results show that the axial stress significantly affects wave velocity, and the relationship between wave

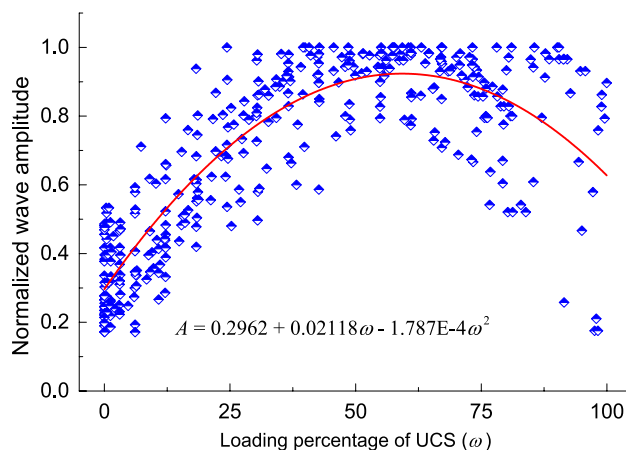


Fig. 4 Change of normalized wave amplitude with compressive loading percentage during compression

velocity (V) and the stress level as a percentage (ω) of UCS can be appropriately characterized by a piecewise function:

$$V_p = \begin{cases} 4902.7 + 175 \cdot \text{LN}(\omega) & 0 < \omega \leq 61 \\ -0.851\omega^2 + 12.408\omega + 5181.86 & 61 \leq \omega \leq 100 \end{cases} \quad (1)$$

Wave velocity increased dramatically when the axial stress increased from 0 MPa to approximately 25% of UCS and continued to increase slightly until the axial

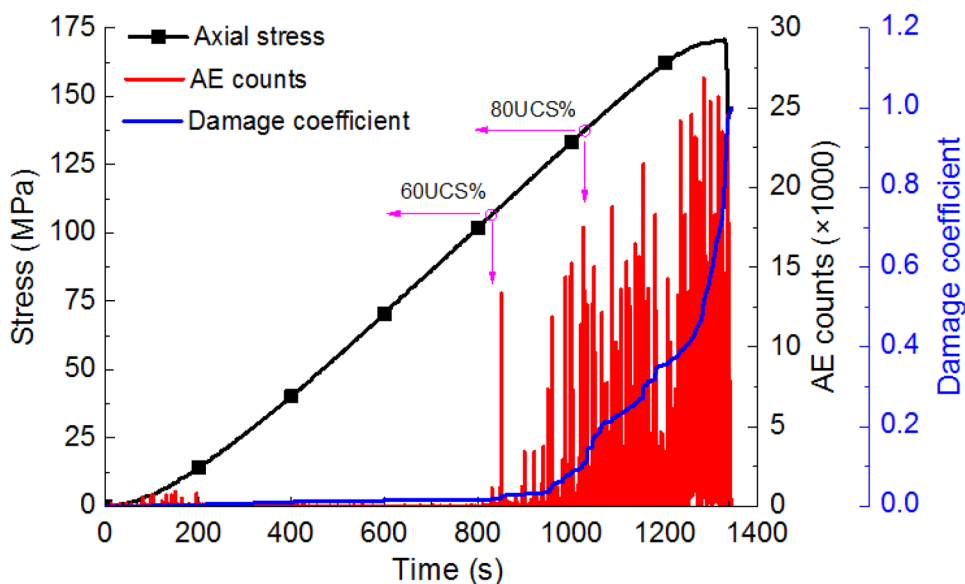
stress reached approximately 60% of UCS. Thereafter, wave velocity remained almost constant and then slightly declined as the axial stress exceeded approximately 90% of UCS. However, wave velocity prior to the peak stress was still much higher than that at the initial loading stage. During loading, the peak wave velocity increased by approximately 20% in average with respect to the initial one without applying loading.

3.1.3 Wave Amplitude

Figure 4 shows the changes of the normalized amplitude of the initial arrival wave under different axial stress levels. Due to the inhomogeneous feature of the granite, the wave amplitude was different from specimen-to-specimen even under the same axial stress level. Therefore, to examine the relationship between wave amplitude and the applied compressive stress, the normalized amplitude was adopted, which is defined as the ratio of individual wave amplitude of a granite specimen under a certain axial stress to the maximum wave amplitude of the specimen measured during loading process. The normalized wave amplitude increased remarkably when the axial stress increased from 0 MPa to approximately 60% of UCS and then decreased with further increase of the axial stress. During the entire loading process, the maximum normalized wave amplitude was nearly tripled with respect to the average initial one without applying stress. The change of the normalized wave amplitude with respect to axial stress can be fitted by a polynomial function:

$$A = 0.2962 + 0.02118\omega - 1.787E - 4\omega^2 \quad (2)$$

Fig. 5 AE activity and damage coefficient characterized by AE counts of a typical specimen (G-23) during uniaxial compression



3.1.4 Acoustic Emission

Figure 5 illustrates the axial stress-time curves and AE activities of a typical granite specimen (G-23) during the entire loading process. AE activity was quiet and inactive before the specimen was loaded to 20% of UCS. At this stage, few AE counts were generated which is due to the closure and compaction of pre-existing microcracks or voids in the specimen at the initial loading stage (Yang and Jing 2011). AE remained inactive during the linear elastic deformation stage when the compressive stress was less than 60% of UCS, implying that few microcracks were created in the specimen at this stage. When the axial stress was greater than 60% of UCS, AE became active and an increasingly more AE events were generated. When the compressive stress exceeded 80% of UCS, AE was continuously generated, and a great number of AE events occurred abruptly with the compressive stress approaching the peak point. This phenomenon suggests that the granite specimen may reach the unstable cracking stage when the compressive stress surpassed 80% of UCS, during which microcracks increased both in number and size, propagated and interacted with each other, eventually coalesced into macro-cracks, and finally leading to brittle failure of the specimens (Eberhardt et al. 1998, 1999; Martin and Chandler 1994).

3.2 Wave Propagation in Granite After Loading

When the axial stress reached the targeted level, the specimens were immediately unloaded. Wave velocity and amplitude through the recovered specimen after unloading were measured afterward to assess the influence of stress-driven damage on wave propagation and attenuation. The changes

in wave velocity (ΔV) and amplitude (ΔA) are, respectively, determined as follows:

$$\Delta V = \frac{V' - V_0}{V_0} \times 100\% \tag{3}$$

$$\Delta A = \frac{A' - A_0}{A_0} \times 100\% \tag{4}$$

where V_0 and V' represent the wave velocity before and after loading, respectively; A_0 and A' refer to the peak amplitude of the initial arrival wave before and after loading, respectively.

Table 2 lists the changes of wave velocity and wave amplitude of the granite specimens before and after loading, where a positive change means an increase of wave velocity or wave amplitude with respect to that of the specimen without loading. Compared with wave velocity before loading, wave velocity of the specimens after loading increased with axial stress and approached the maximum increment of approximately 11% at 87% of UCS. The increment of wave velocity declined to approximately 2.6% when the specimen was loaded to 97% of UCS. Wave velocity of the specimen at failure decreased by approximately 9%. Note that herein the failure specimen refers to the one that is failed into two major blocks and can be approximately spliced together.

When the axial stress increased to 80% of UCS, wave amplitude after loading increased by approximately 21%. Similar to wave velocity, the increment of wave amplitude also declined with further increase in axial stress. However, when the specimens were loaded to 97% of UCS, wave amplitude of the unloaded specimens decreased by approximately 50% with respect to the initial value without loading. Moreover, wave amplitude of the spliced specimens after failure was close to zero, which significantly differs from wave velocity.

4 Analysis

4.1 Damage Evolution During Compression

AE is a process of a sudden release of the stored elastic strain energy resulting from dislocations, microcrack growth, frictional slips, pore collapses, etc. (Eberhardt et al. 1999). Thus, AE signals detected during compressive loading can be applied to characterize damage in rock specimens (Yang et al. 2020a, b; Zhang and Zhou 2020a, b). In this study, AE counts were utilized to quantify damage during the loading process. The damage coefficient is calculated as follows (Liu et al. 2009; Luo et al. 2020; Ohtsu and Watanabe 2001):

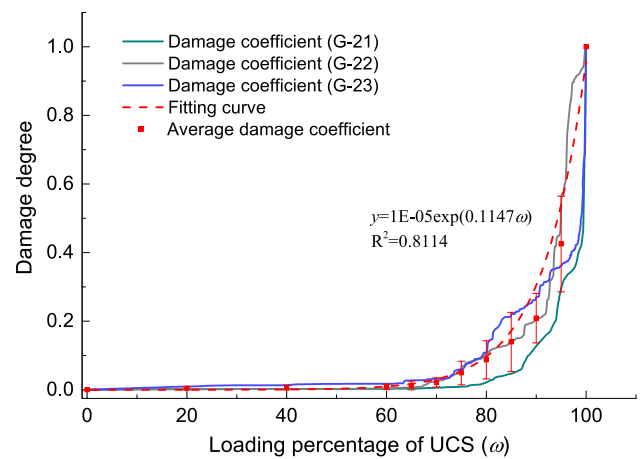


Fig. 6 Relationship between damage coefficient and loading percentage with respect to the UCS

Table 3 Damage coefficients of the failed specimens characterized by AE counts during compression

UCS%	D_{G-21}	D_{G-22}	D_{G-23}	Ave	Std
20	0.0019	0.0018	0.0094	0.0044	0.0044
40	0.0023	0.0024	0.0142	0.0063	0.0068
60	0.0031	0.0047	0.0176	0.0085	0.0080
65	0.0038	0.0077	0.0275	0.0130	0.0127
70	0.0065	0.0260	0.0321	0.0215	0.0134
75	0.0094	0.0720	0.0656	0.0490	0.0344
80	0.0237	0.1110	0.1270	0.0872	0.0556
85	0.0505	0.1450	0.2230	0.1395	0.0864
90	0.1380	0.2070	0.2820	0.2090	0.0720
95	0.3230	0.5840	0.3680	0.4250	0.1395
100	1	1	1	1	0

Ave average value of damage coefficient, Std standard deviation

$$D = \frac{N_A}{N_T} \tag{5}$$

where D is the damage coefficient during compressive loading, N_A is the accumulated AE counts of the specimen loaded to a certain stress level, N_T is the total accumulated AE counts during the entire loading period.

The damage coefficient determined by AE counts of the specimen G-23 during the entire loading process is also shown in Fig. 5. It indicates that AE was inactive before the axial stress reaching 60% of UCS and the damage coefficient was nearly zero. Beyond 60% of UCS, AE became active and the damage coefficient increased. When the axial stress exceeded 80% of UCS and especially approached the peak point, a large number of AE events were detected, and the damage coefficient increased sharply to 1.

Figure 6 presents change of damage coefficient of the failed specimens characterized by AE counts during loading process. It shows that for the completely failed specimens, damage coefficient at any stress level during compression can be determined using the statistical AE counts. Meanwhile, the evolution law of damage coefficient of the failed specimens is consistent, despite a slight deviation prior to the UCS. Therefore, to characterize damage evolution law of granite specimens during uniaxial compression, some damage coefficient values of the failed specimens under different loading stresses were selected for analysis (see Table 3). From Fig. 6, it can be seen that the average damage coefficient was negligible when the compressive stress was below approximately 60% of UCS, and the average damage coefficient of the granite specimen is highly nonlinear under compression and can be fitted by an exponential function:

$$D = 1E - 05\exp(0.1147\omega) \tag{6}$$

4.2 Effect of Damage Evolution on Wave Propagation During Compression

4.2.1 Wave Velocity vs Damage

Figure 7 shows the relationship between wave velocity and damage coefficient during compression. Testing results

show that the dependence of wave velocity on damage during compression can be divided into three stages. At the first stage, when D was less than approximately 0.0025 (the axial stress was approximately 55% of UCS), wave velocity increased sharply. Wave velocity remained nearly constant with D increasing from 0.0025 to approximately 0.315 (the axial stress was approximately 90% of UCS). In the third stage, wave velocity decreased gradually with increasing D . It is seen from Fig. 7 that the results estimated by Eqs. (1 and 6) agree with the testing results, particularly at the first stage. Although there is no second stage reflected by the estimations, the discrepancy is within 3%. Therefore, Eqs. (1 and 6) obtained from the testing results can be used to determine the dependence of wave velocity on damage evolution in the granite specimens during unconfined uniaxial compression.

4.2.2 Wave Amplitude vs Damage

Figure 8 shows the effect of damage on wave amplitude. The results showed that when D was less than 0.0066 (the axial stress was approximately 65% of UCS), wave amplitude increased sharply from approximately 0.3 to 1.0. Subsequently, wave amplitude decreased from the peak to approximately 0.4. The decreasing rate of wave amplitude was accelerated when D was greater than 0.8, i.e., the axial stress was higher than approximately 95% of UCS. Similar to wave velocity, the estimated results by Eqs. (2 and 6) coincide with the testing results, except for the relatively large discrepancy near $D = 1$. Thus, Eqs. (2 and 6) can be

Fig. 7 Relationship between wave velocity and damage coefficient. The points are based on testing results and the dashed line is obtained from Eqs. (1 and 6)

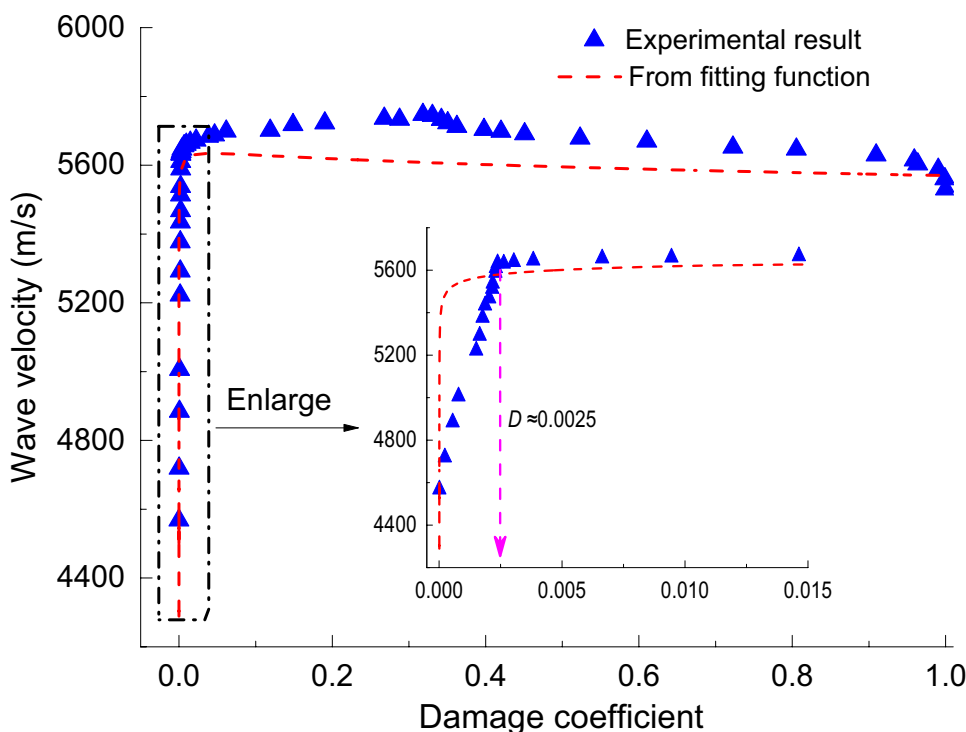


Fig. 8 Relationship between wave amplitude and damage coefficient. The points are based on testing data and the dashed line is determined by Eqs. (2 and 6)

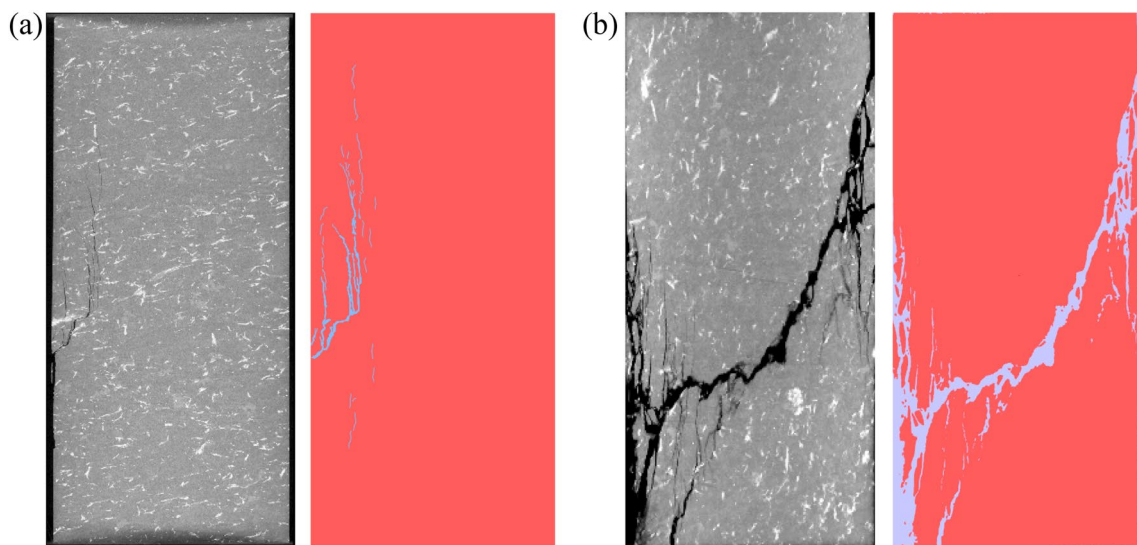
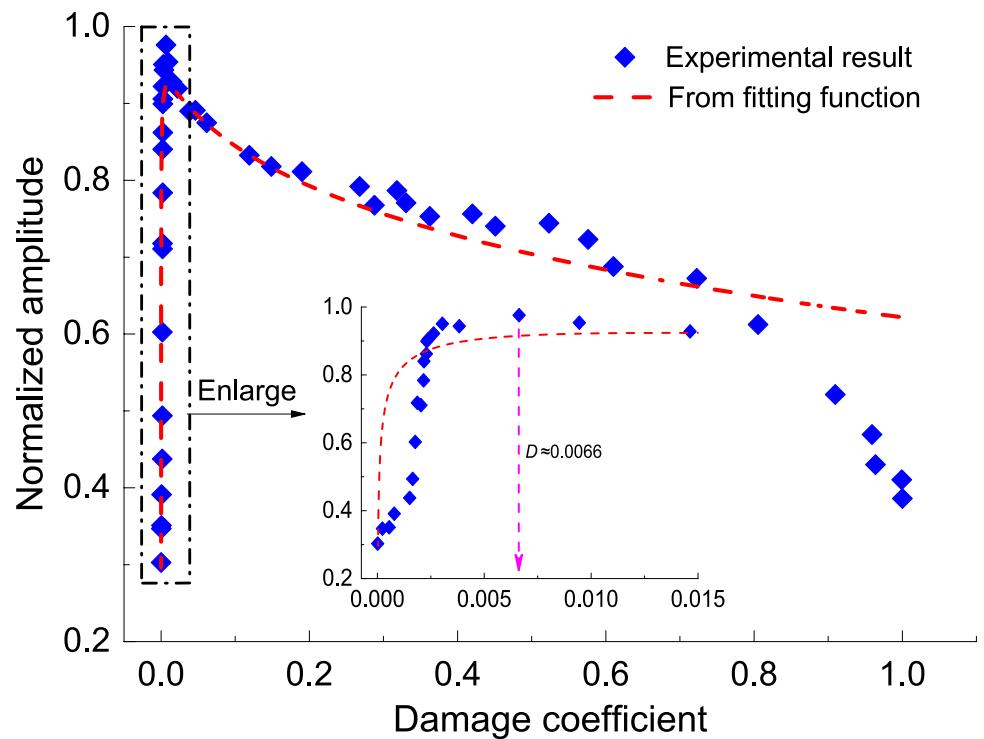


Fig. 9 Micro-CT images and the corresponding cracks of two typical granite specimens subjected to different axial stresses: **a** 97% of UCS; and **b** 100% of UCS. The red and blue colors in the images beside the micro-CT images indicate solid materials and cracks, respectively

used to evaluate the dependence of transmitted wave amplitude on damage in the granite specimens during unconfined uniaxial compression.

4.3 Damage After Compression and its Effect on Wave Propagation

4.3.1 Characterization of Stress-Driven Damage Using Micro-CT

To quantify the stress-driven damage after loading, a Nano-Voxel 2000 micro-CT scanner was used to scan the damaged

specimens at a resolution of $61 \times 61 \times 61 \mu\text{m}^3$. After scanning, a series of micro-CT images were obtained. By setting a proper grayscale threshold in the Avizo software, the micro- and macro-cracks can be appropriately determined by micro-CT images, as shown in Fig. 9. The crack area in each micro-CT image can be statistically calculated by the Avizo software. Based on the continuous damage theory (Kachanov 1986), the stress-driven damage coefficient (D') after loading can be determined (Ma et al. 2016):

$$D' = \frac{1}{n} \sum_{i=1}^n \frac{A'_i}{A_i} \times 100\% \quad (7)$$

where A_i is the area of the i -th micro-CT image of a damaged specimen, A'_i is the total crack area in the i -th micro-CT image, and n is the total number of micro-CT images of the damaged specimen.

To appropriately calculate D' , the crack areas of the damaged specimen, in particular the failed one, must be precisely counted. Fault was observed in the failed specimen, which is formed by large, open cracks and voids rather than dense microcracks, as shown in Fig. 9. The largest aperture of the fault is nearly 2 mm. Therefore, the crack area counted

from the failed specimen will be undoubtedly much greater than the real one. To avoid this problem, the crack areas were counted from some representative regions, which are termed as the characteristic rock elements. This is similar to the treatment in quantifying crack density using representative thin sections obtained from scanning electron microscopy or optical microscopy (Wu et al. 2000). The criteria to select the characteristic rock element are as follows: (1) the element should be near but excluding the fault in the failed specimen; (2) the element should contain sufficient microcracks with at least one or two coalesced cracks that have extended to the element boundary. The first criterion is to avoid the interference of faults, and the second guarantees that the characteristic rock element can be failed by the cracks inside its volume.

Figure 10 illustrates two typical characteristic rock elements extracted from the failed specimen G-23. Two characteristic rock elements were selected in two orthogonal directions parallel and perpendicular to the loading direction. The dimensions of the two elements are $24.4 \times 12.2 \times 12.2 \text{ mm}^3$ and $12.2 \times 12.2 \times 24.4 \text{ mm}^3$, respectively. Based on the method described above, the crack areas of these two characteristic rock elements can be obtained, which are further

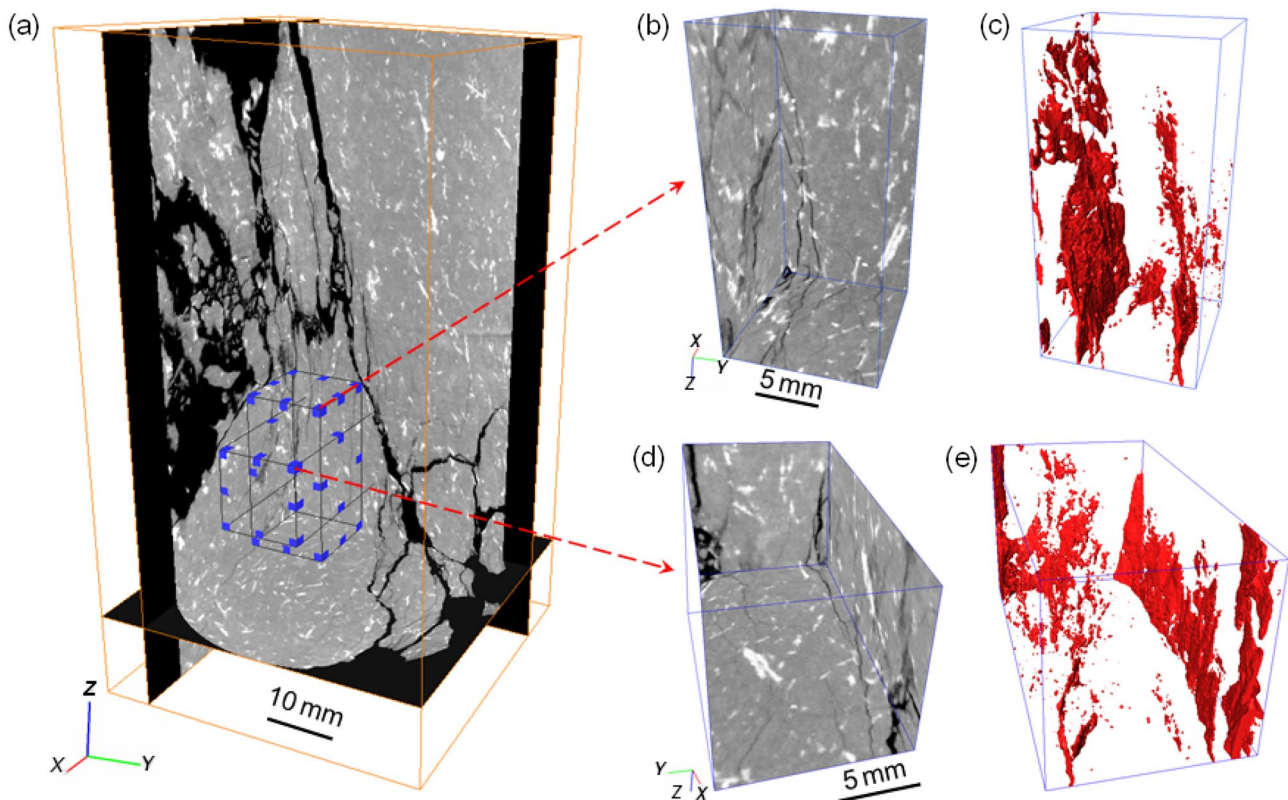


Fig. 10 Determination of cracks from two characteristic rock elements extracted from the failed granite specimen G-23: **a** Exhibition of the locations of the two characteristic rock elements; **b** and **d** the

characteristic rock elements that are parallel and perpendicular to the loading directions, respectively; **c** and **e** cracks (marked by red color) within the characteristic rock elements shown in **b** and **d**, respectively

Table 4 Crack areas and damage coefficient of the damaged rocks

Sample	UCS%	Crack area (mm ²)	Scanning area (mm ²)	D'	D_N
G-4	40	59.17	1,557,009.0	0.0038%	0.002
G-9	60	91.47	1,524,556.7	0.006%	0.0032
G-16	80	730.34	1,587,702.3	0.046%	0.024
G-17	87	2218.13	1,584,381.4	0.14%	0.072
G-20	97	8069.17	1,551,763.5	0.52%	0.268
G-23	100	30,033.96	1,548,142.2	1.94%	1.0

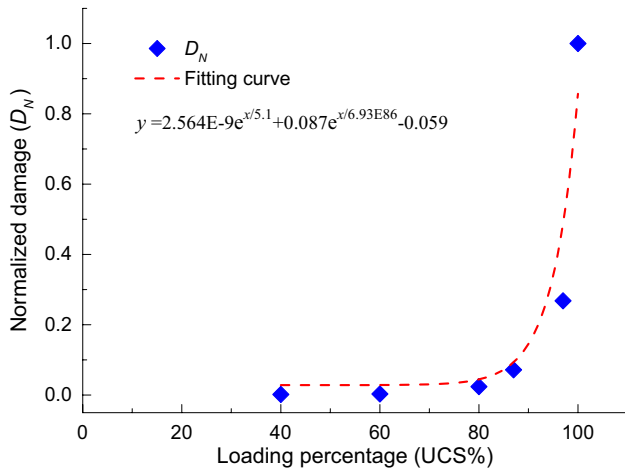


Fig. 11 Normalized damage of the granite after loading vs UCS%

used to determine D' with Eq. (7). D' of the elements along the horizontal and vertical directions are 2.05% and 1.83%, respectively. The average value 1.94% is then used to represent D' of the failed specimen G-23.

Table 4 summarizes the crack areas of damaged rock specimens and D' determined by Eq. (7). In general, the crack areas are small compared to the scanning areas of the entire damaged specimen. When the compressive stress was lower than 60% of UCS, the crack areas generated in the specimen were very small, resulting in a low D' . Similar to the damage coefficient during the loading process characterized by AE counts (see Fig. 6), D' increased with increasing compressive stress and grew sharply to the peak, i.e., 1.94%, when the compressive stress reached the UCS.

For the failed specimen G-23, D' is 1.94%, which is far less than the theoretical predication where damage should be 100% when a material is completely failed (Kachanov 1986). To make D' comparable to damage coefficient during loading process, the normalized damage coefficient D_N is adopted to characterize the stress-driven damage of the granite specimen after loading and unloading processes. D_N is defined as the ratio of D' of the unloaded specimen that has been compacted to a certain load to the peak D' of the failed granite specimen. The change of D_N with respect to the loading percentages after loading and unloading processes

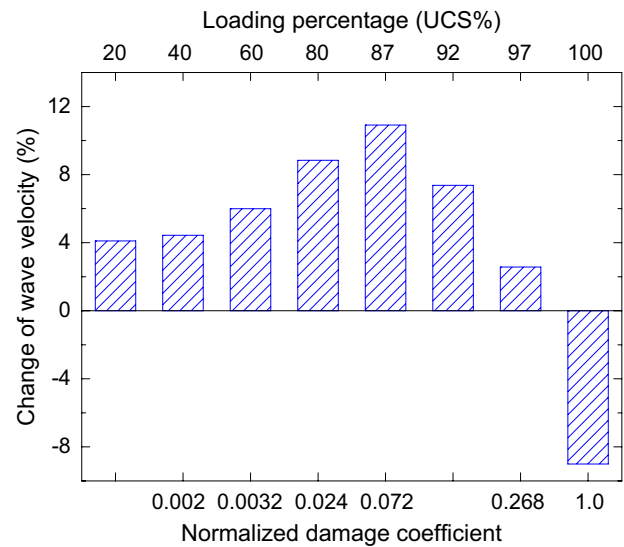


Fig. 12 Relationship between the change of wave velocity and normalized damage coefficient after loading and unloading processes

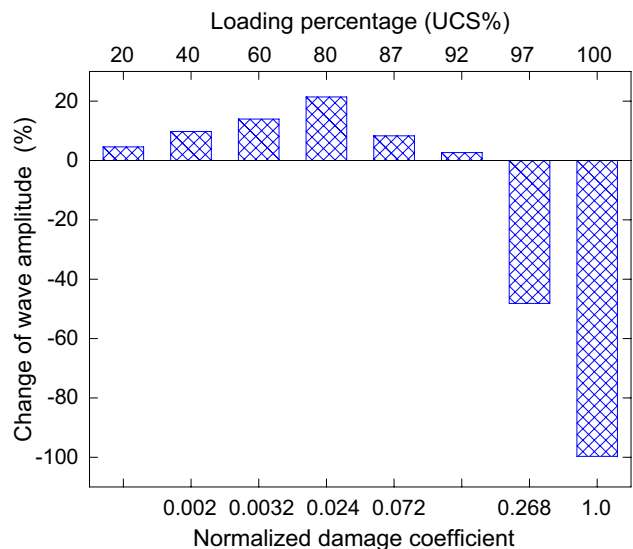


Fig. 13 Relationship between the change of wave amplitude and normalized damage coefficient after loading and unloading processes

is shown in Fig. 11. The result indicates that evolution of D_N is highly nonlinear and can be fitted by an exponential function.

4.3.2 D_N vs Wave Velocity

Figure 12 demonstrates the effect of D_N on the average change of wave velocity after loading and unloading processes, where a positive change means an increase in wave velocity compared with that before loading. Wave velocity of the unloaded specimens is higher than that before loading when the damage coefficient was less than 0.268. Wave velocity of the failed specimen was approximately 9% lower than that before loading. This feature shows that although the stress-driven damage was generated in the specimen, the wave velocity was still higher than the initial velocity before loading if the specimen did not fail. It indicates that the enhancing effect of compaction and closure of cracks on wave velocity of the unloaded specimens was partially retained.

4.3.3 D_N vs Wave Amplitude

The effect of D_N on the average wave amplitude change after loading and unloading processes is presented in Fig. 13. Similar to wave velocity, the compaction and closure of pre-existing cracks and pores in the specimen was not fully recovered after unloading. When D_N is smaller than approximately 0.1, wave amplitude of the unloaded specimens gradually increased with increasing D_N . The maximum increment of wave amplitude was approximately 21% when $D_N = 0.024$. However, when D_N is sufficiently large (e.g., 0.268), wave amplitude of the unloaded specimen was lower than that before loading. For the failed specimen with $D_N = 1.0$, the wave amplitude change was nearly -100%, indicating that the energy of the transmitted wave was almost completely attenuated by the fractures and failed plane within the spliced specimens after failure.

5 Discussion

Testing results showed that wave velocity and the amplitude of the initial arrival wave during compression first increased and then decreased with increasing compressive stress, as shown in Figs. 3 and 4. This is attributed to the combination of two effects on wave propagation, i.e., the enhancing effect due to compaction and closure of initial cracks and the weakening effect resulting from generation of new cracks. When the compressive stress is lower than 60% of UCS, the stress-driven damage is very small, indicating that the weakening effect on wave propagation is negligible. Meanwhile, the application of compressive stress results in the

compaction and closure of pre-existing defects, which leads to the consolidation of contact conditions between individual minerals and change in friction conditions, thereby increasing wave velocity and wave amplitude (Goodfellow et al. 2015; Kaneko et al. 1979; Meredith et al. 1991; Svitek et al. 2017). Because the enhancing effect of compaction and closure of cracks on wave propagation is much stronger than the weakening effect of newly induced damage on wave propagation, the wave velocity and amplitude therefore increase with increasing stress when the compressive stress is lower than 60% of UCS. When the compressive stress is beyond 60% of UCS, dilatancy occurs due to the reopening, generation, propagation and coalescence of microcracks, which induces damage accumulation in the granite specimens, as shown in Fig. 6 (Brace et al. 1966; Goodfellow et al. 2015; Kaneko et al. 1979; Meredith et al. 1991). Consequently, the newly induced damage results in drop of wave velocity and amplitude. In this stage, the weakening effect of newly induced damage played a dominant role on wave propagation. As a result, with increasing compressive stress, wave amplitude and velocity decrease when the compressive stress is higher than approximately 60% and 90% of UCS, respectively.

The variation of wave amplitude with damage is approximately 3~10 times higher than that of wave velocity, suggesting that wave amplitude is much more sensitive to damage than wave velocity. This is because ultrasonic wave can bypass the obstacles such as holes and cracks, and therefore wave velocity is not significantly affected. However, the defects, even the tiny holes and microcracks, in the specimen can significantly dissipate wave energy, thereby causing great attenuation of wave amplitude (Hudson 1981; Johnston et al. 1979). Besides, the particle vibration is also affected by internal friction, which will convert part of wave energy into

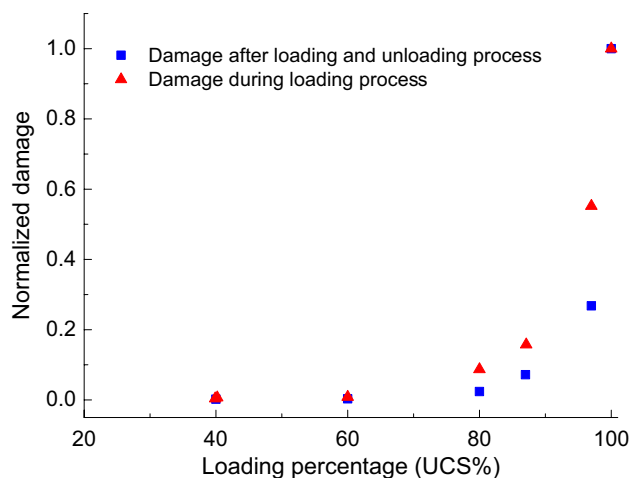


Fig. 14 Comparison of normalized damage coefficients between after loading and unloading processes and during loading process

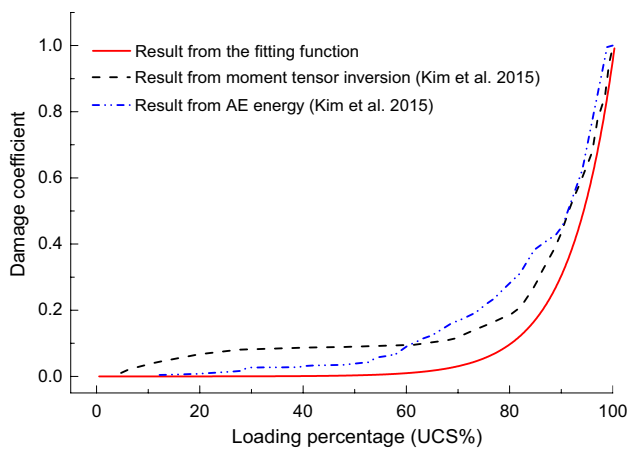


Fig. 15 Comparison of damage coefficients characterized by AE counts in this study with the previous results by Kim et al. (2015)

heat, thus leading to additional wave amplitude attenuation (Tompkins and Christensen 2001; Walsh 1966).

Figure 14 shows the comparison of damage coefficients quantified by AE counts during loading and micro-CT scanning data after loading. In general, the change of damage coefficient characterized by micro-CT scanning data after loading with respect to the loading percentage is similar to that quantified by AE counts during compression. However, when the compressive stress applied to the specimen exceeds 60% of UCS, the damage coefficient of the unloaded specimen was smaller than that during loading process. The damage recovery during unloading is responsible for this phenomenon (Browning et al. 2017; Han 2016; Rao and Ramana 1992). In addition, it should be noted that the damage coefficients during loading and after unloading are determined by different methods, which may also cause this discrepancy. For instance, the resolution of the micro-CT applied for scanning the damaged specimens is 61 μm , which cannot distinguish and detect the microcracks with scales smaller than 61 μm .

Figure 15 gives the comparison of the damage coefficient determined by AE counts in this study with that reported by Kim et al. (2015). The damage coefficients determined by AE counts coincides with those obtained from the moment tensor inversion and AE energy. In particular, the transitions of the normalized stress, i.e., 70%–80% of UCS, for damage evolution during loading are comparable. Therefore, the application of AE counts to quantitatively determine damage during loading is feasible.

Damage evolution may be anisotropic because the stress-driven micro- and macro-cracks tend to propagate along the loading direction under unconfined uniaxial compression (Barnhoorn et al. 2018; Zhou et al. 2018). Therefore, further studies considering anisotropy of damage evolution and its influence on ultrasonic wave propagation along different

directions are needed. In addition, underground rock is often subjected to confining pressures (Ju et al. 2018). Hence, the effect of confining pressure on damage evolution and its influence on wave propagation needs to be studied in the future.

6 Conclusions

The main conclusions are summarized as follows:

- 1) Wave propagation in granite is stress-dependent during compression. However, compared with wave velocity, wave amplitude attenuation is more sensitive to both axial stress and the stress-driven damage.
- 2) The evolution of compressive stress-driven damage in granite specimen is highly nonlinear, it increases drastically to 1.0 with axial stress approaching the peak.
- 3) The increase and decrease of both wave velocity and amplitude during compression are attributed to the combination of two effects on wave propagation, i.e., the enhancing effect due to compaction and closure of initial cracks and the weakening effect resulting from the generation of new cracks.
- 4) The acoustic emission and micro-CT scanning can be adopted to quantify stress-driven damage in granite specimens during and after loading, respectively. The stress-driven damage after unloading is smaller than that during loading.

Acknowledgements We are grateful to Dr. H. Yang from Hong Kong Polytechnic University for her support in processing ultrasonic wave propagation data. This research is financially supported by the Program for Guangdong Introducing Innovative and Entrepreneurial Teams (No. 2019ZT08G315), the Natural Science Foundation of China (No. 52004161, 52274090) and Shenzhen Science and Technology Program (Nos. JCYJ20210324093400001, JCYJ20210324093402006, JCYJ20220818095605012). A portion of this manuscript was reported in a conference (Zhou and Zhu 2018).

Data availability Data will be made available on request.

References

- Abouhussien AA, Hassan AA (2016) Detection of bond failure in the anchorage zone of reinforced concrete beams via acoustic emission monitoring. *Smart Mater Struct* 25(7):075034. <https://doi.org/10.1088/0964-1726/25/7/075034>
- Ahrens TJ, Rubin AM (1993) Impact-induced tensional failure in rock. *J Geophys Res Planets* 98(E1):1185–1203. <https://doi.org/10.1029/92JE02679>
- Ai HA, Ahrens TJ (2007) Effects of shock-induced cracks on the ultrasonic velocity and attenuation in granite. *J Geophys Res Solid Earth* 112(B1):B01201. <https://doi.org/10.1029/2006JB004353>

- Barnhoorn A, Verheij J, Frehner M, Zhubayev A, Houben M (2018) Experimental identification of the transition from elasticity to inelasticity from ultrasonic attenuation analyses. *Geophysics* 83(4):MR221–MR229. <https://doi.org/10.1190/geo2017-0534.1>
- Brace WF, Paulding BW Jr, Scholz CH (1966) Dilatancy in the fracture of crystalline rocks. *J Geophys Res* 71(16):3939–3953. <https://doi.org/10.1029/JZ071i016p03939>
- Browning J, Meredith PG, Stuart CE, Healy D, Harland S, Mitchell TM (2017) Acoustic characterization of crack damage evolution in sandstone deformed under conventional and true triaxial loading. *J Geophys Res Solid Earth* 122(6):4395–4412. <https://doi.org/10.1002/2016JB013646>
- Chaki S, Takarli M, Agbodjan WP (2008) Influence of thermal damage on physical properties of a granite rock: porosity, permeability and ultrasonic wave evolutions. *Constr Build Mater* 22(7):1456–1461. <https://doi.org/10.1016/j.conbuildmat.2007.04.002>
- Chen YL, Wang SR, Ni J, Azzam R, Fernandez-Steeger TM (2017) An experimental study of the mechanical properties of granite after high temperature exposure based on mineral characteristics. *Eng Geol* 220:234–242. <https://doi.org/10.1016/j.enggeo.2017.02.010>
- David C, Menéndez B, Darot M (1999) Influence of stress-driven and thermal cracking on physical properties and microstructure of La Peyratte granite. *Int J Rock Mech Min Sci* 36(4):433–448. [https://doi.org/10.1016/S0148-9062\(99\)00010-8](https://doi.org/10.1016/S0148-9062(99)00010-8)
- Eberhardt E, Stead D, Stimpson B, Read RS (1998) Identifying crack initiation and propagation thresholds in brittle rock. *Can Geotech J* 35(2):222–233. <https://doi.org/10.1139/t97-091>
- Eberhardt E, Stead D, Stimpson B (1999) Quantifying progressive pre-peak brittle fracture damage in rock during uniaxial compression. *Int J Rock Mech Min Sci* 36(3):361–380. [https://doi.org/10.1016/S0148-9062\(99\)00019-4](https://doi.org/10.1016/S0148-9062(99)00019-4)
- Feng XT, Chen S, Zhou H (2004) Real-time computerized tomography (CT) experiments on sandstone damage evolution during triaxial compression with chemical corrosion. *Int J Rock Mech Min Sci* 41(2):181–192. [https://doi.org/10.1016/S1365-1609\(03\)00059-5](https://doi.org/10.1016/S1365-1609(03)00059-5)
- Goodfellow SD, Tisato N, Ghofranitabari M, Nasser MHB, Young RP (2015) Attenuation properties of Fontainebleau sandstone during true-triaxial deformation using active and passive ultrasonics. *Rock Mech Rock Eng* 48(6):2551–2566. <https://doi.org/10.1007/s00603-015-0833-8>
- Han T (2016) A simple way to model the pressure dependency of rock velocity. *Tectonophysics* 675:1–6. <https://doi.org/10.1016/j.tecto.2016.03.008>
- Han ZY, Li DY, Zhou T, Zhu QQ, Ranjith PG (2020) Experimental study of stress wave propagation and energy characteristics across rock specimens containing cemented mortar joint with various thicknesses. *Int J Rock Mech Min Sci* 131:104352. <https://doi.org/10.1016/j.ijrmms.2020.104352>
- Huang S, Xia K, Zheng H (2013) Observation of microscopic damage accumulation in brittle solids subjected to dynamic compressive loading. *Rev Sci Instrum* 84(9):093903. <https://doi.org/10.1063/1.4821497>
- Huang XL, Qi SW, Guo SF, Dong WL (2014) Experimental study of ultrasonic waves propagating through a rock mass with a single joint and multiple parallel joints. *Rock Mech Rock Eng* 47(2):549–559. <https://doi.org/10.1007/s00603-013-0399-2>
- Hudson JA (1981) Wave speeds and attenuation of elastic waves in material containing cracks. *Geophys J Int* 64(1):133–150. <https://doi.org/10.1111/j.1365-246X.1981.tb02662.x>
- Iturrioz I, Lacidogna G, Carpinteri A (2013) Acoustic emission detection in concrete specimens: experimental analysis and lattice model simulations. *Int J Damage Mech* 23(3):327–358. <https://doi.org/10.1177/1056789513494232>
- Johnston DH, Toksöz MN, Timur A (1979) Attenuation of seismic waves in dry and saturated rocks: II. Mechanisms. *Geophysics* 44(4):691–711. <https://doi.org/10.1190/1.1440969>
- Ju Y, Xie H, Zheng Z, Lu J, Mao L, Gao F, Peng RD (2014) Visualization of the complex structure and stress field inside rock by means of 3D printing technology. *Chin Sci Bull* 59(36):5354–5365. <https://doi.org/10.1007/s11434-014-0579-9>
- Ju Y, Xi C, Zhang Y, Mao L, Gao F, Xie H (2018) Laboratory in situ CT observation of the evolution of 3D fracture networks in coal subjected to confining pressures and axial compressive loads: a novel approach. *Rock Mech Rock Eng* 51(11):3361–3375. <https://doi.org/10.1007/s00603-018-1459-4>
- Kachanov L (1986) Introduction to continuum damage mechanics, vol 10. Springer Science & Business Media, Berlin
- Kaneko K, Inoue I, Sassa K, Ito I (1979) Monitoring the stability of rock structures by means of acoustic wave attenuation. *Proceedings 4th Congress of ISRM*. pp: 287–292.
- Kawakata H, Cho A, Kiyama T, Yanagidani T, Kusunose K, Shimada M (1999) Three-dimensional observations of faulting process in Westerly granite under uniaxial and triaxial conditions by X-ray CT scan. *Tectonophysics* 313(3):293–305. [https://doi.org/10.1016/S0040-1951\(99\)00205-X](https://doi.org/10.1016/S0040-1951(99)00205-X)
- Kim JS, Lee KS, Cho WJ, Choi HJ, Cho GC (2015) A comparative evaluation of stress–strain and acoustic emission methods for quantitative damage assessments of brittle rock. *Rock Mech Rock Eng* 48(2):495–508. <https://doi.org/10.1007/s00603-014-0590-0>
- Li JC, Li HB, Zhao J (2015) An improved equivalent viscoelastic medium method for wave propagation across layered rock masses. *Int J Rock Mech Min Sci* 73:62–69. <https://doi.org/10.1016/j.ijrmms.2014.10.008>
- Liu C, Ahrens TJ (1997) Stress wave attenuation in shock-damaged rock. *J Geophys Res Solid Earth* 102(B3):5243–5250. <https://doi.org/10.1029/96JB03891>
- Liu BX, Huang JL, Wang ZY, Liu L (2009) Study on damage evolution and acoustic emission character of coal-rock under uniaxial compression. *Chin J Rock Mech Eng* 28(S1):3234–3238 (**in Chinese**)
- Luo DN, Su GS, Zhang GL (2020) True-triaxial experimental study on mechanical behaviours and acoustic emission characteristics of dynamically induced rock failure. *Rock Mech Rock Eng* 53:1205–1223. <https://doi.org/10.1007/s00603-019-01970-x>
- Ma T, Yang C, Chen P, Wang X, Guo Y (2016) On the damage constitutive model for hydrated shale using CT scanning technology. *J Nat Gas Sci Eng* 28:204–214. <https://doi.org/10.1016/j.jngse.2015.11.025>
- Martin CD, Chandler NA (1994) The progressive fracture of Lac du Bonnet granite. *Int J Rock Mech Min Sci* 31(6):643–659. [https://doi.org/10.1016/0148-9062\(94\)90005-1](https://doi.org/10.1016/0148-9062(94)90005-1)
- Martínez-Martínez J, Fusi N, Galiana-Merino JJ, Benavente D, Crosta GB (2016) Ultrasonic and X-ray computed tomography characterization of progressive fracture damage in low-porous carbonate rocks. *Eng Geol* 200:47–57. <https://doi.org/10.1016/j.enggeo.2015.11.009>
- Meredith PG, Ayling MR, Murrell SAF, Sammonds PR (1991) Cracking, damage and fracture in stressed rock: a holistic approach. In: Shah SP (ed) *Toughening mechanisms in quasi-brittle materials*. Kluwer Academic Publishers, Dordrecht, pp 67–89
- Modiriasari A, Pyrak-Nolte LJ, Bobet A (2018) Emergent wave conversion as a precursor to shear crack initiation. *Geophys Res Lett* 45(18):9516–9522. <https://doi.org/10.1029/2018GL078622>
- Ohtsu M, Watanabe H (2001) Quantitative damage estimation of concrete by acoustic emission. *Constr Build Mater* 15(5–6):217–224. [https://doi.org/10.1016/S0950-0618\(00\)00071-4](https://doi.org/10.1016/S0950-0618(00)00071-4)

- Pyrak-Nolte LJ, Myer LR, Cook NGW (1990) Transmission of seismic waves across single natural fractures. *J Geophys Res Solid Earth* 95:8617–8638. <https://doi.org/10.1029/JB095iB06p08617>
- Rao MVMS, Ramana YV (1992) A study of progressive failure of rock under cyclic loading by ultrasonic and AE monitoring techniques. *Rock Mech Rock Eng* 25(4):237–251. <https://doi.org/10.1007/BF01041806>
- Renard F, Bernard D, Desrues J, Ougier-Simonin A (2009) 3D imaging of fracture propagation using synchrotron X-ray microtomography. *Earth Planet Sci Lett* 286(1):285–291. <https://doi.org/10.1016/j.epsl.2009.06.040>
- Shatilo AP, Sondergeld C, Rai CS (1998) Ultrasonic attenuation in Glenn Pool rocks, northeastern Oklahoma. *Geophysics* 63(2):465–478. <https://doi.org/10.1190/1.1444348>
- Shirole D, Hedayat A, Walton G (2020) Illumination of damage in intact rocks by ultrasonic transmission-reflection and digital image correlation. *J Geophys Res Solid Earth*. 125(7):e2020JB019526. <https://doi.org/10.1029/2020JB019526>
- Stanchits S, Vinciguerra S, Dresen G (2006) Ultrasonic velocities, acoustic emission characteristics and crack damage of basalt and granite. *Pure Appl Geophys* 163(5–6):975–994. <https://doi.org/10.1007/s00024-006-0059-5>
- Svitek T, Vavryčuk V, Lokajčiek T, Petružálek M, Kern H (2017) Effect of pressure on 3D distribution of P-wave velocity and attenuation in antigorite serpentinite. *Geophysics* 82(4):WA33–WA43. <https://doi.org/10.1190/geo2017-0006.1>
- Tapponnier P, Brace WF (1976) Development of stress-induced microcracks in Westerly granite. *Int J Rock Mech Min Sci* 13(4):103–112. [https://doi.org/10.1016/0148-9062\(76\)91937-9](https://doi.org/10.1016/0148-9062(76)91937-9)
- Tompkins MJ, Christensen NI (2001) Ultrasonic P- and S-wave attenuation in oceanic basalt. *Geophys J Int* 145(1):172–186. <https://doi.org/10.1046/j.0956-540x.2001.01354.x>
- Walsh JB (1966) Seismic wave attenuation in rock due to friction. *J Geophys Res* 71(10):2591–2599. <https://doi.org/10.1029/JZ071i010p02591>
- Wu XY, Baud P, Wong TF (2000) Micromechanics of compressive failure and spatial evolution of anisotropic damage in darley dale sandstone. *Int J Rock Mech Min Sci* 37(1–2):143–160. [https://doi.org/10.1016/S1365-1609\(99\)00093-3](https://doi.org/10.1016/S1365-1609(99)00093-3)
- Wu W, Lu DZ, Elsworth D (2022) Fluid injection-induced fault slip during unconventional energy development: a review. *Energy Rev* 1(2):100007. <https://doi.org/10.1016/j.enrev.2022.100007>
- Xi DY, Qiu WL, Cheng JY, Yi LK, Zhang B, Xie D (1997) Relation between attenuation and porosity or saturation of rock. *Oil Geophys Prospect* 32(2):196–201 (**in Chinese**)
- Xie HP, Zhu JB, Zhou T, Zhang K, Zhou CT (2020) Conceptualization and preliminary study of engineering disturbed rock dynamics. *Geomech Geophys Geo-Energy Geo-Resour* 6:34. <https://doi.org/10.1007/s40948-020-00157-x>
- Yang SQ, Jing HW (2011) Strength failure and crack coalescence behavior of brittle sandstone samples containing a single fissure under uniaxial compression. *Int J Fract* 168(2):227–250. <https://doi.org/10.1007/s10704-010-9576-4>
- Yang GS, Xie DY, Zhang CQ (1998) The quantitative analysis of distribution regulation of CT values of rock damage. *Chin J Rock Mech Eng* 17(3):279–285 (**in Chinese**)
- Yang SQ, Ranjith PG, Jing HW, Tian WL, Ju Y (2017) An experimental investigation on thermal damage and failure mechanical behavior of granite after exposure to different high temperature treatments. *Geothermics* 65:180–197. <https://doi.org/10.1016/j.geothermics.2016.09.008>
- Yang H, Duan HF, Zhu JB (2020a) Effects of filling fluid type and composition and joint orientation on acoustic wave propagation across individual fluid-filled rock joints. *Int J Rock Mech Min Sci* 128:104248. <https://doi.org/10.1016/j.ijrmms.2020a.104248>
- Yang J, Mu ZL, Yang SQ (2020b) Experimental study of acoustic emission multi-parameter information characterizing rock crack development. *Eng Fract Mech* 232:107045. <https://doi.org/10.1016/j.engfracmech.2020b.107045>
- Zhang JZ, Zhou XP (2020a) Forecasting catastrophic rupture in brittle rocks using precursory ae time series. *J Geophys Res Solid Earth*. 125:e2019JB019276. <https://doi.org/10.1029/2019JB019276>
- Zhang JZ, Zhou XP (2020b) AE event rate characteristics of flawed granite: from damage stress to ultimate failure. *Geophys J Int* 222(2):795–814. <https://doi.org/10.1093/gji/ggaa207>
- Zhang Z, Zhang R, Xie H, Liu J, Were P (2015) Differences in the acoustic emission characteristics of rock salt compared with granite and marble during the damage evolution process. *Environ Earth Sci* 73(11):6987–6999. <https://doi.org/10.1007/s12665-015-4406-7>
- Zhao J, Cai JG, Zhao XB, Li HB (2006) Experimental study of ultrasonic wave attenuation across parallel fractures. *Geomech Eng* 1(2):87–103. <https://doi.org/10.1080/1748620600834613>
- Zhou T, Zhu JB (2018) Monitoring of damage evolution in granite under uniaxial compression by AE and Wave velocity. *Rock dynamics and applications theories and applications*. CRC Press, New York, pp 77–81
- Zhou T, Dong SL, Zhao GF, Zhang R, Wu SY, Zhu JB (2018) An experimental study of fatigue behavior of granite under low-cycle repetitive compressive impacts. *Rock Mech Rock Eng* 51:3157–3166. <https://doi.org/10.1007/s00603-018-1515-0>
- Zhou T, Zhu JB, Ju Y, Xie HP (2019) Volumetric fracturing behavior of 3D printed artificial rocks containing single and double 3D internal flaws under static uniaxial compression. *Eng Fract Mech* 205:190–204. <https://doi.org/10.1016/j.engfracmech.2018.11.030>
- Zhu ZM, Xie HP, Mohanty B (2008) Numerical investigation of blasting-induced damage in cylindrical rocks. *Int J Rock Mech Min Sci* 45(2):111–121. <https://doi.org/10.1016/j.ijrmms.2007.04.012>
- Zhu JB, Perino A, Zhao G, Barla G, Li JC, Ma GW, Zhao J (2011) Seismic response of a single and a set of filled joints of viscoelastic deformational behaviour. *Geophys J Int* 186(3):1315–1330. <https://doi.org/10.1111/j.1365-246X.2011.05110.x>
- Zhu JB, Zhou T, Liao ZY, Sun L, Li XB, Chen R (2018) Replication of internal defects and investigation of mechanical and fracture behaviour of rock using 3D printing and 3D numerical methods in combination with X-ray computerized tomography. *Int J Rock Mech Min Sci* 106:198–212. <https://doi.org/10.1016/j.ijrmms.2018.04.022>
- Zhu JB, Zhai TQ, Liao ZY, Yang SQ, Liu XL, Zhou T (2020) Low-amplitude wave propagation and attenuation through damaged rock and a classification scheme for rock fracturing degree. *Rock Mech Rock Eng* 53(9):3983–4000. <https://doi.org/10.1007/s00603-020-02162-8>

Publisher's Note Springer Nature remains neutral with regard to jurisdictional claims in published maps and institutional affiliations.

Springer Nature or its licensor (e.g. a society or other partner) holds exclusive rights to this article under a publishing agreement with the author(s) or other rightsholder(s); author self-archiving of the accepted manuscript version of this article is solely governed by the terms of such publishing agreement and applicable law.